TECHNICAL ARTICLE

Sampling volumes in powder diffraction experiments

M. Alican Noyan [1] and I. Cevdet Noyan [2,a)]
[1]Department of Applied Data Science and Artificial Intelligence, Breda University of Applied Sciences, Mgr. Hopmanstraat 2, Breda, The Netherlands
[2]Department of Applied Physics and Applied Mathematics, SEAS, Columbia University, 116th St. and Broadway, New York, NY 10027, USA

(Received 7 May 2024; accepted 10 September 2024)

We present a simple analytical formalism based on the Lorentz-Scherrer equation and Bernoulli statistics for estimating the fraction of crystallites (and the associated uncertainty parameters) contributing to all finite Bragg peaks of a typical powder pattern obtained from a static polycrystalline sample. We test and validate this formalism using numerical simulations, and show that they can be applied to experiments using monochromatic or polychromatic (pink-beam) radiation. Our results show that enhancing the sampling efficiency of a given powder diffraction experiment for such samples requires optimizing the sum of the multiplicities of reflections included in the pattern along with the wavelength used in acquiring the pattern. Utilizing these equations in planning powder diffraction experiments for sampling efficiency is also discussed.

[doi:10.1017/S0885715624000484]

Keywords: powder diffraction, sampling statistics, Lorentz sampling equation, Scherrer equation

I. INTRODUCTION

Powder diffraction patterns from polycrystalline aggregates are routinely analyzed to obtain quantitative, phase-specific crystallographic and structural parameters such as volume fractions, crystallographic orientation distributions, lattice parameters, atomic occupancy factors, crystallite sizes, strain and "micro-strain" values, atomic positions, and space groups (Bijvoet et al., 1969; Azâroff, 1974; Klug and Alexander, 1974; Cheary et al., 2004). The crystallographic and structural parameters obtained from these analyses are (diffraction) averages of their respective distributions within the material volume subset contributing finite intensity to the measured pattern. Consequently, it is of interest to estimate the fraction of diffracting crystallites contributing to a powder pattern. There is a limited number of articles discussing this issue in past literature. The seminal analysis was published by Alexander et al. (1948) where the Lorentz sampling equation (Buerger, 1940; Buerger and Klein, 1945) and Bernoulli statistics (Uspensky, 1937; Johnson et al., 2005) were utilized to determine the fraction of crystallites contributing to a given reflection, and its uncertainty parameters, for a stationary powder sample. These variables were then used to estimate the expected diffraction intensities and their associated uncertainties. For experimental verification, the authors measured diffracted intensities for the 3.33 Å quartz powder reflection [$(10\bar{1}1)$ and $(01\bar{1}1)$ planes] for four sets of samples with grain sizes in the range of 15–50, 5–50, 5–15, and <5 μm, and reported reasonable agreement with the analytically predicted results (Unfortunately, terms such as particle size, average particle size, and particle size distribution etc. depend on the technique used for their determination and are not well defined for arbitrary particle shapes or characterization techniques. Different techniques usually yield quite different results. Disagreements are also encountered when one compares crystallite sizes obtained from different diffraction formulations (Noyan and Öztürk, 2022). In the current manuscript the terms "grain size", "crystallite size", and "particle size" are used interchangeably and follow the usage of the original authors.). De Wolff (1959) published an extended theoretical analysis, where expressions for the relative r.m.s. error of diffractometer intensity measurements due to sampling statistics were derived for stationary and spinning samples; the results obtained for stationary specimens were essentially identical with the result derived by Alexander et al. (1948). These equations were then tested and verified by acquiring experimental data from silicon powder specimens with crystallite sizes between 30 and 50 μm; here, the dependence of the standard deviation of measured intensities on X-ray wavelengths was also studied. It was reported that higher energy X-ray beams sampled more grains due to deeper penetration and had better intensity statistics (De Wolff et al., 1959). In 1970, Jenkins and De Vries included a (solved)

a)Author to whom correspondence should be addressed. Electronic mail: icn2@columbia.edu

question on the effect of (diffractometer) particle statistics on measured intensities in "Worked Examples in X-Ray Analysis" (Jenkins and de Vries, 1978). Smith (1991, 2001) singled out particle statistics as the most severe limitation on the (potential) accuracy of Rietveld refinement of powder diffraction patterns measured on laboratory-based diffractometers with standard optics, using, mostly, Cu $K\alpha$ radiation. He identified an upper limit powder crystallite size of 1 μm; only diffraction patterns of powder samples with grain sizes equal to, or lower than, this value, could be refined with reproducible results. Elton and Salt (1996) extended the formulations by Alexander et al. (1948) and De Wolff (1959) by considering the effects of Soller slits in the incident and/or diffracted beam paths. They showed that, for powder samples with crystallite sizes around 8 μm, the contribution of the fractional particle-statistics error to the uncertainty of the (measured) diffracted (integrated) intensity of the (112) quartz line could be an order of magnitude larger than the uncertainty predicted by counting statistics alone. (In current practice, Rietveld full-pattern refinement codes only consider counting statistics; They do not explicitly report estimated diffracting grain fractions. This practice can cause errors in the interpretation of the results.) Ida and co-workers used the formulations by Alexander et al. (1948) and De Wolff (1959) to link the uncertainty in measured diffraction intensities caused by particle statistics in a spinner-scan method to evaluate particle sizes in crystalline powder samples (Ida et al., 2009). They reported that effective crystallite diameters larger than 5 μm could be evaluated by statistical analysis of diffraction intensity data collected by stepwise rotation of a flat powder specimen on a laboratory Bragg-Brentano powder diffractometer. In a later paper, they showed that smaller crystallite sizes could be measured on a synchrotron source due to the availability of higher incident intensities (Ida et al., 2011). There were also earlier studies where the Lorentz sampling equation and its extensions had been used to determine particle sizes (Schdanow, 1935; Taylor, 1961).

In contrast to the majority of references discussed above, where the number of diffracting particles was inferred from measured intensities, Noyan and Kaldor (2004) utilized a synchrotron micro-beam scanning technique to directly count the number of diffracting grains for various reflections, when an annealed Cu strip with a mean optical grain size of 29 ± 8 μm was irradiated with monochromatic X-rays. Their results showed that, for all studied reflections, the fraction of strongly diffracting grains in an area of approximately 4 mm^2 was less than 0.2% of all grains illuminated by the X-ray beam, indicating very marked under-sampling. They also reported that the Lorenz sampling equation predicted much lower diffracting grain fractions when the optically measured grain size was used in this formulation, indicating that, even for annealed ductile specimens, the optical and X-ray "grain sizes" were not identical. In a series of recent articles, Noyan and co-workers (Öztürk et al., 2014, 2015; Öztürk and Noyan, 2017) extended the analysis by Alexander et al. (1948) to nanocrystalline powder samples using modeling, and showed that this classic formalism yielded erroneous results for powder samples with crystallite sizes below 100 nm. These errors increased with decreasing particle size and became very significant for particles smaller than 10 nm since one of the fundamental assumptions used by Alexander et al. (1948) is not valid below this size (Öztürk et al., 2014).

Our literature review, summarized above, showed that most past articles in this area focused on the errors caused in measured diffracted intensities due to sampling statistics. The effects of scanning geometry, incident and diffracted optics of various types, incident beam divergence, depth-of-penetration of the incident radiation, and other instrumental parameters on the shape and volume of the illuminated volume have been extensively discussed, but there has been little work on determining the fraction, or population, of diffracting crystallites. However, quantifying the fraction of diffracting grains for a particular reflection, or for all reflections of a powder pattern utilized in a refinement, can be quite useful: this describes the specimen volume contributing information to the measured signal during the experiment and can be used to evaluate sampling efficiency. This can be of particular importance if the data are measured from a stationary, solid polycrystalline sample examined for directional properties, such as lattice strain along a given sample direction. In such cases, the sample cannot be ground into a powder and rotated. Further, if the measured strains are then used with bulk elastic moduli to compute the stress tensor in the illuminated volume, it is implicitly assumed that the sampled volume is greater than the (continuum mechanics) representative volume element of the particular material (Şeren et al., 2023). This assumption must be validated to avoid errors in computed stresses.

In what follows, we present a simple analytical formalism based on the combined Lorentz-Scherrer equation (Öztürk et al., 2014, 2015; Öztürk and Noyan, 2017) for estimating the fractions of kinematically diffracting crystallites, and their uncertainty, for all finite Bragg peaks of a powder pattern. These equations are valid for sample sizes between 100 nm and the (lower) dynamical scattering size limit (Authier, 2003) and utilize easily accessible parameters. We test and validate this formalism using numerical simulations and discuss its utilization in planning powder diffraction experiments.

II. THEORY

We start with a basic review of the relevant definitions and equations based on previous work (Alexander et al., 1948; Öztürk et al., 2014, 2015; Öztürk and Noyan, 2017).

Consider an ideal powder ensemble of perfect (defect-free) single crystallites, infinite in number, all of which are identical in shape, size, composition, and crystal symmetry. We assume that these crystals are small enough to diffract in the kinematical regime, i.e., primary and secondary extinction effects can be neglected, and are randomly oriented in direct space. From this ensemble Y specimens, each with N_G crystallites, $\{N_G\}_i$, $i \in (1, Y)$, are taken, and their diffraction patterns are recorded one after another using monochromatic, plane-wave incident X-rays with wavelength λ. Here, we assume that all N_G crystallites within a sample are illuminated by the X-ray beam, and the X-rays from all diffracting crystallites can reach the detector utilized in the experiment. (These conditions are best approximated in high-energy synchrotron experiments utilizing area detectors.) Due to the random orientations of the constituent crystallites in direct space the populations of crystallites diffracting into a given hkl reflection, $\{\{N^*_{hkl}\}\}$, for the set of samples, $\{\{N_G\}\}$, will be randomly distributed around the same expected value, $E[N^*_{hkl}]$. Since,

https://doi.org/10.1017/S0885715624000484 Published online by Cambridge University Press

within each $\{N_G\}_i$, a crystallite is either diffracting (state one) or not diffracting, (state zero), the expected population of crystals oriented properly for diffraction into a given *hkl* reflection, $E[N^*_{hkl}]$, its variance, $V[N^*_{hkl}]$, standard deviation, $S[N^*_{hkl}]$, and relative standard deviation (RSD), $u[N^*_{hkl}]$ (also termed "the coefficient of variation"), are described by the (discrete) Bernoulli probability distribution (Uspensky, 1937; Johnson et al., 2005):

$$E[N^*_{hkl}] = N_G p^*_{hkl} \tag{1}$$

$$V[N^*_{hkl}] = N_G q^*_{hkl} p_{hkl} \tag{2}$$

$$S[N^*_{hkl}] = (V[N^*_{hkl}])^{1/2} \tag{3}$$

$$u[N^*_{hkl}] = \left(\frac{q^*_{hkl}}{N_G p^*_{hkl}}\right)^{1/2} \tag{4}$$

where the starred terms denote diffraction variables; p^*_{hkl} is the probability that a given (randomly oriented) crystallite will contribute finite intensity, statistically exceeding the local background, to the *hkl* reflection centered at the Bragg angle $\theta_{B,hkl}$; q^*_{hkl} is the corresponding complementary probability, $q^*_{hkl} = (1 - p^*_{hkl})$.

The diffraction probability, p^*_{hkl}, in Eqs. (1)–(4) depends on the crystallographic properties of the diffracting crystallites and the diffraction geometry. For the experimental configuration shown in Figure 1, all crystallites that exactly satisfy Bragg's law for an *hkl* reflection will have poles (intersections of *hkl* vectors normal to the diffracting planes with the surface of the unit sphere) on the *hkl* reflection circle. This circle is the locus of the poles of all vectors making the (complementary) angle $\Gamma_B = (\pi/2) - \theta_B$ with the incident beam, $\vec{k}_o$. The locus of the intersections of the diffracted beam vectors, $(\vec{k}_{d,\theta_B})_j$, with the unit sphere surface is the Debye circle for the *hkl* reflection; all points on this circle are at $2\theta_B$ from the transmitted beam, $\vec{k}_t$. In this geometry, $\widehat{2\theta}$ varies from 0° to 180°, while $\hat{\Gamma}$ varies from 90° to 0°.

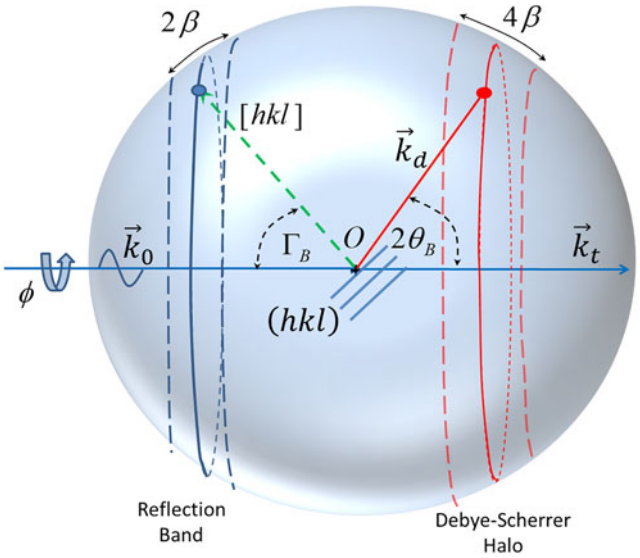

Figure 1. Diffraction geometry used in the simulations. The monochromatic incident beam, $\vec{k}_0$, impinges on the (*hkl*) planes of a crystallite satisfying the diffraction condition, and produces the diffracted beam, $\vec{k}_d$, and the transmitted beam, $\vec{k}_t$. There is 360° rotational symmetry around $\vec{k}_d$, $\vec{k}_t$. The central circles of the two spherical zones are the loci of the intersections of all diffracting plane normal vectors, [*hkl*], and diffracted beam vectors, $\vec{k}_d$, of crystals oriented for perfect diffraction. All poles within the reflection band correspond to diffracted beams with finite intensity within the Debye-Scherrer halo (the detection band).

For the ideal experiment with a perfect powder sample, the intensities of diffracted beams decrease symmetrically and monotonically with their angular deviation, $|\delta 2\theta|$, from the exact Bragg condition, decaying to background at a limiting deviation of $\pm\Delta 2\theta/2$; that is, for any diffracted beam of finite intensity, $-(\Delta 2\theta/2) < \delta 2\theta < (\Delta 2\theta/2)$. Each of these diffracted beams originates from a specific crystallite with an (active) *hkl* pole within the "reflection band", defined as the spherical band of angular width $\Delta\theta$ centered on the reflection circle at Γ_B. Based on this construct, the probability p^*_{hkl} is identified as the probability that an [*hkl*] vector from a particular crystallite intersects the unit sphere surface within the reflection band of the *hkl* reflection.

We note that the above discussion can be cast in strictly geometric form (without involving diffraction): The probability, $p_{\theta,\Delta\theta}$, that a given random vector $\vec{V}$, intersects the unit sphere surface within a particular spherical band of arbitrary width, $\Delta\theta_A$, centered around an arbitrary angle, $\Gamma_A = (\pi/2) - \theta_A$, is equal to the fractional area of this band:

$$p_{\theta,\Delta\theta} = \frac{1}{2}\cos\theta_A \sin\Delta\theta_A \cong \frac{1}{2}\cos\theta_A \Delta\theta_A \tag{5}$$

Using this geometric probability, the expected number of poles, $E[N_P^{\theta_A,\,\Delta\theta_A}]$, of an arbitrary population of randomly oriented vectors, N_V, within a spherical band described by the arbitrary angular parameters, θ_A, $\Delta\theta_A$, and its dispersion parameters, can be obtained from Eqs. (1)–(4):

$$E[N_P^{\theta_A,\,\Delta\theta_A}] = \frac{1}{2} N_V \cos\theta_A \Delta\theta_A \tag{6}$$

$$S[N_P^{\theta_A,\,\Delta\theta_A}] = (N_V\, p_{\theta_A,\,\Delta\theta_A}\, q_{\theta_A,\,\Delta\theta_A})^{1/2} \cong \left(\frac{N_V \cos\theta_A\, \Delta\theta_A}{2}\right)^{1/2} \tag{7}$$

$$u[N_P^{\theta_A,\,\Delta\theta_A}] = \left(\frac{q_{\theta_A,\Delta\theta_A}}{N_V\, p_{\theta_A,\,\Delta\theta_A}}\right)^{1/2} \cong \left(\frac{\cos\theta_A \Delta\theta_A}{2N_V}\right)^{1/2} \tag{8}$$

Here the approximate equations are valid for small $\Delta\theta_A$.

In powder diffraction, the probability, p^*_{hkl}, that a particular crystallite contributes finite intensity to the reflection at Bragg angle, $\theta_{B,hkl}$, is given by the product of the fractional area of the *hkl* reflection band on the unit sphere surface, and the multiplicity, m_{hkl}, of this reflection:

$$p^*_{hkl} \cong \frac{1}{2} m_{hkl} \cos\theta_{B,hkl} \Delta\theta_{hkl} \tag{9}$$

This is the classical Lorentz probability equation for a stationary sample (Buerger, 1940; Buerger and Klein, 1945; Cullity, 1978) which shows that, for a constant reflection band breadth, $\Delta\theta_{hkl}$, p^*_{hkl} decreases with Bragg angle, and tends to zero for full back-reflection geometry, $\theta_{B,hkl} \to (\pi/2)$.

One can obtain the expected population of crystals oriented properly for diffraction into a given *hkl* reflection, and its uncertainty parameters, by combining Eqs. (1)–(4) and (9).

https://doi.org/10.1017/S0885715624000484 Published online by Cambridge University Press

However, the probability, p^*_{hkl}, described by Eq. (9) corresponds strictly to the fraction of *hkl* poles expected in the corresponding reflection circle. This would be equal to the fraction of diffracting crystallites if, and only if, each diffracting crystallite contributes only one pole to the *hkl* reflection band. In this case, the expected number of crystallites diffracting in a particular reflection can be expressed as (This equality is exactly satisfied for infinitesimal reflection band breadths, $\Delta\theta_{hkl}$.):

$$E[N_{G^*}^{\theta_B,\,\Delta\theta_{hkl}}] \cong E[N_{P^*}^{\theta_B,\,\Delta\theta_{hkl}}] \tag{10}$$

The standard deviation, $S[N_{G^*}^{\theta_B,\,\Delta\theta_{hkl}}]$, and RSD, $u[N_{G^*}^{\theta_B,\,\Delta\theta_{hkl}}]$, of $E[N_{G^*}^{\theta_B,\,\Delta\theta_{hkl}}]$ can be obtained substituting Eq. (9) in Eqs. (6)–(8).

In the diffraction process the breadth of the reflection band, $\Delta\theta_{hkl}$, is not arbitrary, but strictly defined by contributions from both the specimen and the instrument used in the experiment. In the ideal experiment we describe here there is no instrumental broadening, and the specimen contribution, $\Delta\theta^{Sp}_{hkl}$, is defined by the band-pass of the crystallite for a permitted reflection. For a perfect crystallite of size D, $\Delta\theta^{Sp}_{hkl}$ is related to the full-width at half maximum (FWHM) of the diffraction peak, β, via the Scherrer equation (For unstrained single crystals scattering in the kinematic regime, the crystallite size obtained from the Scherrer equation is the maximum real-space length of the coherently scattering domains along the scattering wavevector (Noyan and Öztürk, 2022). We term this parameter the "Scherrer (crystallite) size".):

$$\beta = \frac{K_{Sr}\lambda}{D\cos\,\theta} \tag{11}$$

Thus, the breadth of the reflection band becomes:

$$\Delta\theta^{Sp}_{hkl} = \frac{s\beta}{2} = \frac{sK_{Sr}\lambda}{2D\cos\,\theta} \tag{12}$$

Here K_{Sr} is the Scherrer shape factor with a value around 0.9, and s is a (numeric) range factor which specifies the angular breadth (in terms of β) over which the diffraction peaks are recorded. For radial scans with a Gaussian peak-shape, setting $s = 4$, will capture over 99% of the integrated intensity of the peak (Öztürk et al., 2015).

From Eqs. (5) and (12), we obtain the (combined) Scherrer-Lorentz probability for activated poles:

$$p^*_{hkl} = K'\left(\frac{m_{hkl}\lambda}{D}\right), \quad K' = \frac{sK_{Sr}}{2} \tag{13}$$

Then, the expected value of activated poles contributing to any *hkl* reflection, and its dispersion parameters are given by:

$$E[N_{P^*}^{\theta_B,\,\Delta\theta_{hkl}}] = K'N_G\left(\frac{m_{hkl}\lambda}{D}\right) \tag{14}$$

$$S[N_{P^*}^{\theta_B,\,\Delta\theta_{hkl}}] = (N_G\,p_{hkl}\,q_{hkl})^{1/2} \cong \left(\frac{K'N_G m_{hkl}\lambda}{D}\right)^{1/2} \tag{15}$$

$$u[N_{P^*}^{\theta_B,\,\Delta\theta_{hkl}}] \cong \left(\frac{D}{K'N_G m_{hkl}\lambda}\right)^{1/2} \tag{16}$$

Equations (13)–(16) have no dependency on the diffraction angle, θ_B, and show that, for a given powder pattern, only the multiplicity term, m_{hkl}, determines the ratio of the diffraction volumes of various reflections (The diffraction volume of a given reflection is defined as the product of the crystallite volume, assumed to be the same of all crystallites in our analysis, and the number of diffracting crystallites.). For example, for a powder sample consisting of equal-sized crystallites with cubic symmetry, the ratio of crystallites contributing to *h*00 and *hk*0 peaks would be 1:4, independent of their Bragg angles. We also observe that, all other factors being equal, increasing the size of the crystallites decreases the expected number of diffracting crystallites, $E[N_{P^*}^{\theta_M,\,\Delta\theta}]$, and increases its RSD, $u[N_{P^*}^{\theta_M,\,\Delta\theta}]$ (Here, per Eq. (14), we are assuming that the number of activated poles is equal to the number of diffracting crystallites.). This results from the decrease in the acceptance angle [Eq. (12)] of the crystallites with increasing size, which reduces the diffraction probability, p^*_{hkl} [Eq. (13)].

Using Eq. (14), the expected total number of diffracting crystallites contributing to the powder pattern, $E[N^{*ptn}_{tot}]$, is obtained as a sum over all finite reflections in the measurement:

$$E[N^{*ptn}_{tot}] = \sum_i K'N_G\left(\frac{m_{(hkl)_i}\lambda}{D}\right) = K''\,C_\lambda, \qquad K'' = \frac{K'N_G}{D} \tag{17}$$

Here C_λ, the sampling parameter, is defined as the product of the wavelength, λ, used to acquire the pattern, and the sum of multiplicities of all finite reflections included in the powder pattern analysis:

$$C_\lambda = \lambda\sum_i m_{(hkl)_i} \tag{18}$$

Equation (17) shows that experimentally maximizing $E[N^{*ptn}_{tot}]$ is an optimization problem: this value is linearly proportional to the sampling parameter, C_λ [Eq. (18)]. However, for experiments utilizing monochromatic radiation, one needs to decrease λ to increase the number of observed reflections. Thus, from a strictly crystallite sampling perspective, decreasing λ from 1.5 to 0.1 Å to obtain more reflections would enhance crystallite sampling only if $\sum_i m_{(hkl)_i}$ at the shorter wavelength (higher energy) is 15 times larger.

The standard deviation, $S[N^{*ptn}_{tot}]$, and RSD, $u[N^{*ptn}_{tot}]$, for $E[N^{*ptn}_{tot}]$ can be obtained from the variances, $V[N_{hkl}]$ [Eq. (2)] of all finite reflections:

$$S[N^{*ptn}_{tot}] \cong \left(\frac{K'N_G}{D}C_\lambda\right)^{1/2} \tag{19}$$

$$u[N^{ptn}_{tot}] \cong \left(\frac{D}{K'N_G C_\lambda}\right)^{1/2} \tag{20}$$

As expected, an increase in the sampling parameter, C_λ, decreases the RSD of $E[N^{ptn}_{tot}]$.

https://doi.org/10.1017/S0885715624000484 Published online by Cambridge University Press

For a given specimen, the change in sampling efficiency when the experiment wavelength is changed from λ_1 to λ_2 can be quantified using a sampling quotient $Q^S_{\lambda_1\to\lambda_2}$:

$$Q^S_{\lambda_1\to\lambda_2} = \frac{E[N^{ptn}_{tot}]_{\lambda 2}}{E[N^{ptn}_{tot}]_{\lambda 1}} = \frac{\lambda_2 \sum_j m_{(hkl)_j}}{\lambda_1 \sum_i m_{(hkl)_i}} = \frac{C_{\lambda_2}}{C_{\lambda_1}} \qquad (21)$$

Sampling is enhanced if $Q^S_{\lambda_1\to\lambda_2} > 1$.

If one estimates the total number of crystallites, N_G, in the beam for a given experiment, Eqs. (17)–(20) can be used to calculate the number of crystallites with Scherrer crystallite sizes, D, contributing to the powder pattern. If this population is deemed inadequate, one can increase the number of reflections used in the powder pattern analysis, or use Eq. (21) to choose a wavelength that would provide better sampling. In what follows, we test these predictions using Monte Carlo modeling.

III. MONTE CARLO SIMULATIONS

These simulations were limited to powder samples consisting of crystallites with (coherently scattering) Scherrer sizes, D, larger than 100 nm since our previous work showed that Eqs. (14)–(16) are not applicable for particle sizes in the nano-regime (Öztürk et al., 2014, 2015; Öztürk and Noyan, 2017). We used two sets of simulations: In the first set, which is strictly based on geometry, we compared three different approaches for simulating the number of poles in an angular interval, $\Delta\theta$, as a function of its central position, θ, to identify the most efficient modeling approach with acceptable precision. These three approaches were, in order, (1) completely uncorrelated, randomly oriented vectors; (2) randomly oriented sets of correlated families of vectors from one reflection, *hkl* (such as families of crystallographic directions from randomly oriented grains); and (3) sets of correlated vectors from multiple reflections for all randomly oriented crystals. (To make the problem computationally tractable, we included only the first five reflections in simulations based on the third approach.) We note that only the first case satisfies the assumptions made in deriving the classical Lorentz equation.

In the second set of simulations, we applied the procedure determined above by introducing diffraction selectivity.

A. Geometric analysis

1. Uncorrelated vectors

These models satisfy all assumptions of the Lorentz-Bernoulli formalism. Here, we generated sets of vectors $\{N_V\}$, $N_V \in (600, 24\,000\,000)$, all originating from a single point, O, which were oriented randomly in direct (Cartesian) space [Figure 2(a)]. We tested these sets to verify that their orientations were random (We used the Mathematica "SpectralRandomnessTest" function for this purpose (https://resources.wolframcloud.com/FunctionRepository/resources/SpectralRandomnessTest).), and then counted the number of poles (intersections) falling within bands of constant breadth, $\Delta\theta = 0.5$ (0.0087 radians), across the entire reflection half-sphere [Figure 2(b)], with $\theta \in (0.25^\circ, 89.75^\circ)$. Multiple independent sets were generated for each population, N_V, to obtain statistical distributions. These results were, then, compared with calculated values from Eqs. (6) and (7).

In Figure 3, the number of poles falling into each reflection band is plotted, along with the area fraction of each band [Eq. (6), right ordinate] for 30 independent simulations, each with $N_V = 5000$. We observe that, for a fixed band breadth, $\Delta\theta = 0.5$, the fraction of poles decreases monotonically from approximately 0.42% to 0.1% for Bragg angles between 15° to 150° 2θ. For $N_V = 5000$, this corresponds to 25 to 5 poles per band, respectively. Also, while the averages and standard deviations of 30 instances (i.e., averaging over 150 000 independent vectors) for these bands are quite close to the predictions of Eqs. (6) and (7), these equations are quite

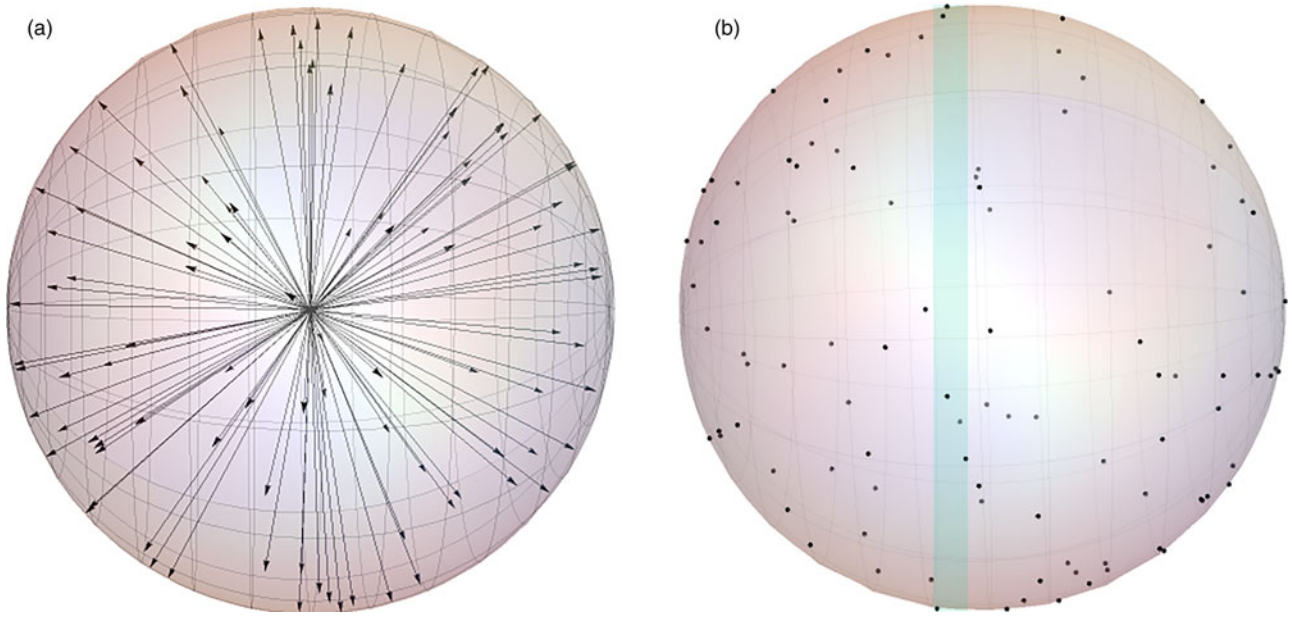

Figure 2. A random distribution of vectors within a unit sphere (a) and their intercepts on the sphere surface (b) used for testing the geometric analysis described by Eqs. (5)–(8). The pole populations for various reflection bands, such as the shaded band in (b), are numerically determined and compared with the expected values obtained from the analytical equations.

https://doi.org/10.1017/S0885715624000484 Published online by Cambridge University Press

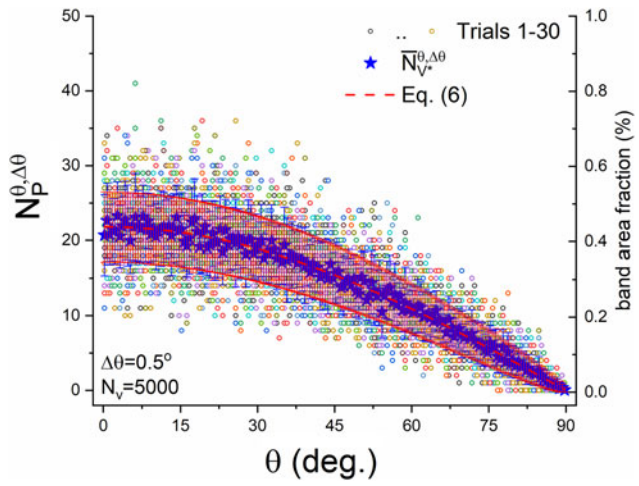

Figure 3. The number of poles in each reflection band, $\Delta\theta = 0.5$, $0.25 \leq \theta \leq 88.75$, for 30 independent simulations, each with 5000 random vectors. The average values and the expected number of intercepts, $E[N_{V^*}^{\theta,\Delta\theta}]$, are also shown. The red dashed line also shows the area fraction of each band [Eq. (6)] when the right ordinate is used.

imprecise in predicting the number of poles and their dispersion in any band for any independent instance with $N_V = 5000$.

To quantify the effect of N_V on the distribution of poles in a given interval, $N_P^{\theta_M,\Delta\theta}$, we obtained the RSD, $u[N_P^{\theta,\Delta\theta}]$, for seven populations where $N_V \in [600,\ 24\,000\,000]$. For each population, 10 instances were simulated. The results are summarized in Figure 4. We observe good agreement between the numerical model values and the analytical computations. We also observe that, for each band centered at θ_M, $\log(u[N_P^{\theta_M,\Delta\theta}])$ decreases linearly with $\log(N_V)$ with a slope equal to $-(1/2)$. This can be predicted by using Eqs. (5) and (8):

$$\log(u[N_P^{\theta_M,\Delta\theta}]) \cong -\frac{1}{2}(\log(p_{\theta_M,\Delta\theta}) + \log(N_V)) \qquad (22)$$

Figure 4 shows that, for a fixed band breadth, $\Delta\theta$, large N_V are required to minimize the RSD, $u[N_{V^*}^{\theta_M,\Delta\theta}]$, over the entire angular (θ) range. A population of 1 000 000 vectors or greater

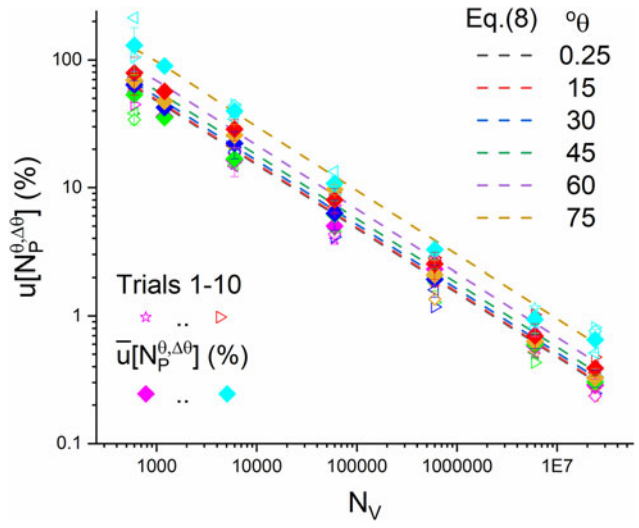

Figure 4. Variation of the RSD of vector intercepts, $(\boldsymbol{u}[N_{V^*}^{\theta_A,\Delta\theta}])$, with set population, N_V, for several arbitrary band-center angles, θ_A. For all cases , $\Delta\theta = 0.5$. The dashed lines depict the values predicted by Eq. (8).

was required to obtain $u[N_{V^*}^{\theta,\Delta\theta}]$ less than 5% for any band of width $\Delta\theta = 0.5°$ in the angular range $\theta \in [0, 75°]$.

2. Uncorrelated families of (correlated) vectors

For this set of simulations, we assumed a cubic crystal and substituted a family of crystal directions, $\langle hkl \rangle$, with m_{hkl} correlated vectors for each (randomly oriented) vector $\vec{V}_i$ in Figure 2(a). For example, in the case of the $\langle h00 \rangle$ family, each $\vec{V}_i$ was replaced by the [001] direction of a particular family, and all other $\langle 100 \rangle$ vectors, at the specific orientations dictated by the (cubic) crystal symmetry, were also added. Thus, any model with N_G crystallites possessed $N_V = m_{hkl}.N_G$ vectors. For these models, as expected, our tests indicated non-random distributions of poles on the unit sphere surface; while the orientations of "families-of-vectors" associated with each $\vec{V}_i$ were uncorrelated, the orientations of $\langle hkl \rangle$ vectors associated with a given $\vec{V}_i$ were non-random.

Figure 5 shows the number of $\langle h00 \rangle$ poles falling into each reflection band, $\Delta\theta = 0.5°$, $0.25° \leq \theta \leq 88.75°$, obtained for 10 independent simulations, each with 600 crystallites (N_G), corresponding to 3600 [h00] directions (N_V). The results exhibit some scatter due to the small N_V. However, if we compare the expected number of intercepts, $E[N_{h00}^*]$, computed from Eq. (6) for 3600 random vectors, with the overall simulation average, $\overline{N}_{h00}^*$, we observe acceptable statistical agreement.

3. Correlated families of (correlated) vectors

For this set of simulations, we assigned the crystal direction [001] to each (randomly oriented) vector $\vec{V}_i$ in Figure 2(a), and then added all vectors belonging to "j" families of crystal directions, $\langle hkl \rangle_j$ to the model at the proper angular coordinates dictated by crystal symmetry. Thus, each crystal contributed "j" correlated crystal direction families, each with m_{hkl_j} correlated vectors. For a model with N_G crystallites, the number of poles distributed on the surface of the unit sphere was $N_G \sum_j m_{hkl_j}$. Our tests showed that this distribution was also non-random. We note that, even though a given reflection

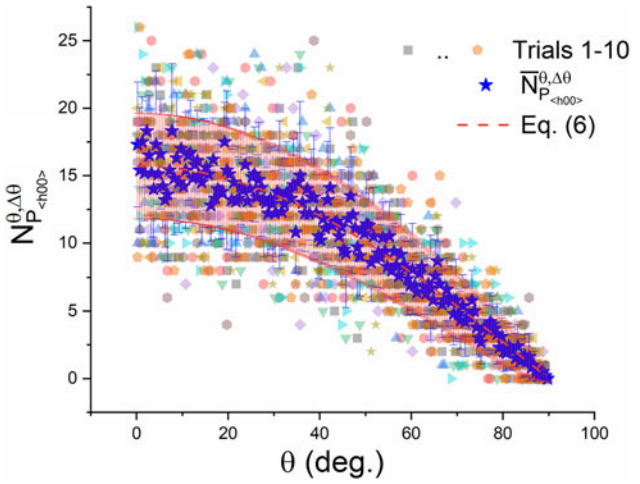

Figure 5. $\langle h00 \rangle$ pole population in each reflection band, $\Delta\theta = 0.5°$; $0.25° \leq \theta \leq 88.75°$, obtained from 10 independent simulations, each with 600 crystallites (N_G). The average pole populations, their standard deviation, as well as the expected number of poles (dashed line) and its standard deviation for each band are also shown.

https://doi.org/10.1017/S0885715624000484 Published online by Cambridge University Press

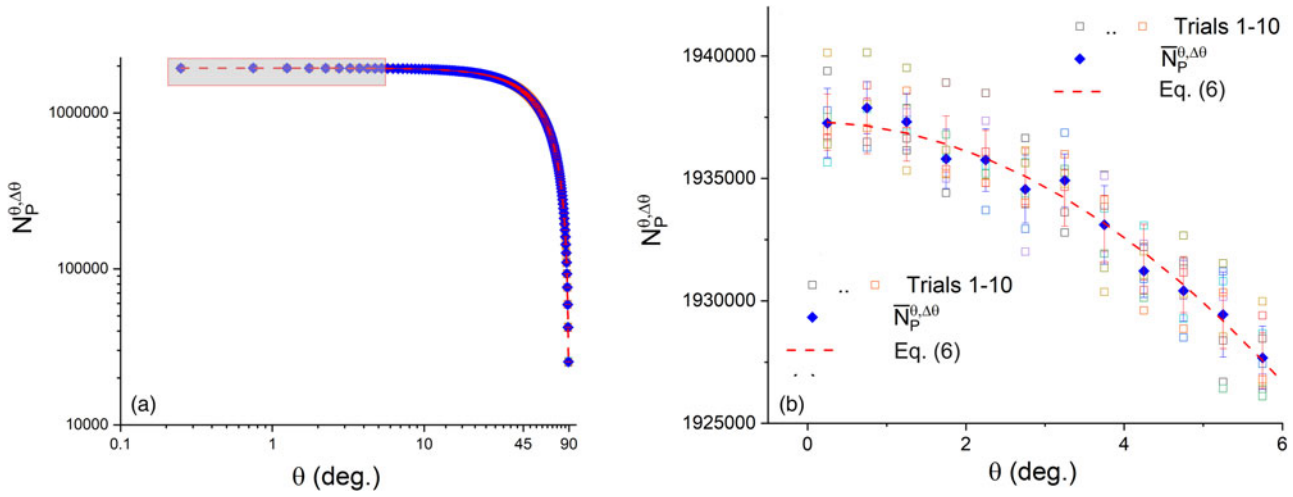

Figure 6. (a) Variation of total pole population of the first five basis-permitted vectors of a diamond cubic crystal in each reflection band, $\Delta\theta = 0.5°$, in the range $0.25° \le \theta \le 88.75°$, obtained for 10 independent instances, each with 6 000 000 crystallites. The average values for each interval, the expected values from Eq. (6), and their standard deviation are also shown. The data in the shaded rectangle is plotted with linear axes in (b), which also depicts the legend for both figures.

band contains poles from many families of crystal directions, only the poles belonging to the particular reflection satisfy Bragg's law, and are, thus, active poles, with corresponding diffracted beams in the particular reflection band.

In Figure 6(a), we plot the variation of total vector intercepts for the first five basis-permitted vectors of a diamond cubic crystal, $N_{V^*}^{\theta,\Delta\theta} = N_{111}^* + N_{220}^* + N_{311}^* + N_{400}^* + N_{331}^*$, falling into equi-angle reflection bands, $\Delta\theta = 0.5°$, in the range $0.25° \le \theta \le 88.75°$, obtained for 10 independent simulations, each with 6 000 000 crystallites (N_G). The average values for each interval from the simulation, the expected values for non-correlated vectors computed from Eq. (6), and their respective standard deviations are also shown. Because of the very large number of crystal vectors (and poles), Figure 6(a) is presented as a log–log plot to facilitate comparison of the simulated and predicted values over the entire θ range. We observe good agreement. This is better illustrated in Figure 6(b), where the shaded range in Figure 6(a) is plotted with linear axes. In this range, the differences between predicted and simulated (average) pole populations are less than 0.02%. We conclude that all reflection populations, N_{hkl}^*, and their dispersions, could be predicted using Eqs. (6) and (7).

The results summarized in Figures 5 and 6 show that the classical formalism based on the Bernoulli statistics [Eqs. (6)–(8)] and the Lorentz sampling equation [Eq. (9)], while strictly applicable only to the case of uncorrelated vectors in Cartesian space (Figures 2 and 3), is also adequate for predicting the pole density within a reflection band and its dispersion parameters when there is:

1. crystallographic orientation correlation between lattice vectors of any given ⟨*hkl*⟩ family for a particular grain, while the orientation of this family is uncorrelated with the orientations of all other vector families, or
2. crystallographic orientation correlation between all lattice vectors belonging to a given crystallite, while orientations of individual grains are uncorrelated.

Thus, both of these approaches are suitable for modeling the number of crystallites contributing to a given diffraction pattern; both sets of simulations yield results very close to the expected values and standard deviations predicted using Eqs. (6) and (7), respectively. We note that, since these equations do not take into account the angular relationships between poles of a given family, or between poles of different families, the geometric approach is valid for modeling crystallites of arbitrary symmetry. In what follows, we utilize the second approach, where the crystallographic correlations between lattice vectors of a given family are maintained while the angular distribution of families of directions are uncorrelated, for modeling the diffracting grain fractions from ensembles of Si crystallites. The third case, where all relevant reflections were modeled together, with the geometrically required angular relationships between their poles, required significantly larger computing power and much longer run times, while yielding identical results with the second approach.

B. Diffraction pattern modeling

1. Monochromatic simulations

This set of simulations was conducted to study the effects of incident beam wavelength on diffraction sampling. In the simulations, plane-wave, monochromatic Cr, Cu, or Mo$K\alpha$ X-rays were specified. For each wavelength activated pole populations of permitted reflections from ideal Si powders for a set of Scherrer sizes (D) were modeled. For all cases we assumed $s = 4$, ensuring that the reflection band captured 99% of the integrated intensity of the peak, and N_G =6 000 000, which yielded less than 2% RSD for all reflections over the angular range of interest (Figure 4). The number of vectors for each reflection, $N_{V_{hkl}}$, had values between 36×10^6 and 288×10^6 for (basis-permitted) *h*00 and *hkl* reflections, respectively. The parameters used in these simulations are listed in Table I. In Figures 7(a)–7(c), we show example powder patterns for the three wavelengths used in our simulations. These patterns were computed with the HighScore Suite (Degen et al., 2014), assuming an infinite number of crystallites in the sample.

For most of these simulations, the FWHM (β_{hkl}) values of the Bragg peaks, computed from the Scherrer equation [Eq. (11)], are significantly smaller [Figures 8(a)–8(c) for Cr, Cu,

https://doi.org/10.1017/S0885715624000484 Published online by Cambridge University Press

TABLE I. Monte Carlo simulation parameters.

Hypothetical sample		Si powder	
Lattice parameter (Å)		5.430941	
Scherrer constant (K_{Sr})		0.9	
Scherrer sizes (nm)		100, 150, 200, 250, 300, 350, 450	
Powder sample population (N_G)		6 000 000	
Range parameter (s)		4	
Angular range ($^\circ\theta$)		0.25–88.75	
Radiation	Cr (λ_1)	Cu (λ_2)	Mo (λ_3)
Wavelength (Å)	2.2909	1.54059	0.71075
# of reflections in pattern	5	12	19

and Mo radiations, respectively] than the fixed reflection band breadth, $\Delta\theta = 0.5^\circ$, used in the geometric analysis. During modeling, the reflection half-sphere was divided into sub-bands of angular width 0.001° to facilitate efficient numerical analysis; the total number of activated poles for a given reflection was obtained by summing over all sub-bands within the relevant reflection band. (Since the sub-band breadth selected was much smaller than the width of the narrowest reflection bands, this simplification resulted in trivial errors in the simulation results.)

In Figures 9(a)–9(c), the variation of diffracting crystallite fractions with Scherrer crystallite size are shown for individual reflections, $(N_G^*/N_G)_{hkl}$, for simulations with Cr, Cu, and Mo

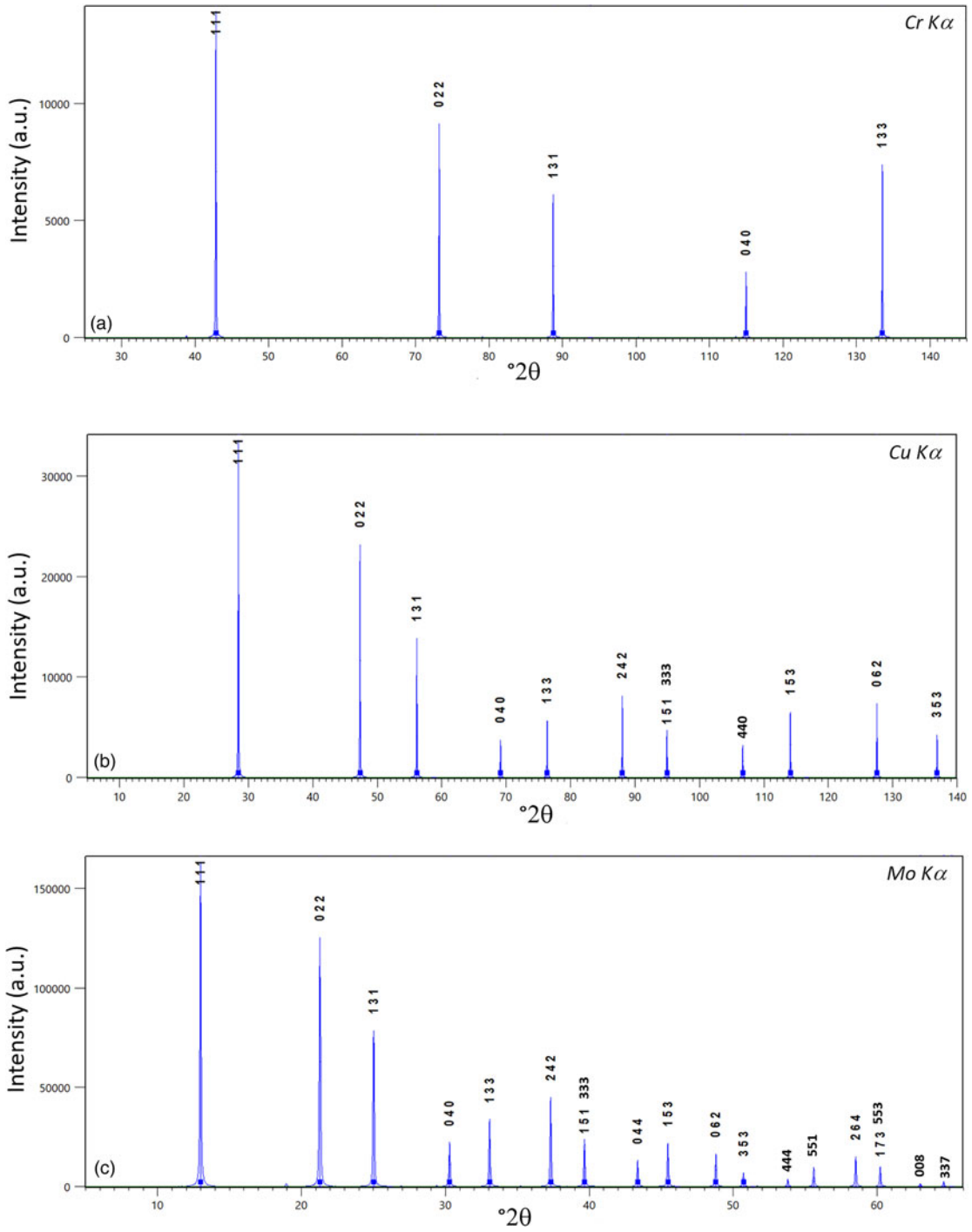

Figure 7. Silicon powder patterns simulated with monochromatic Cr (a), Cu (b), and Mo (c) $K\alpha$ radiations using X'Pert HighScore Plus V4.8 software (Degen et al., 2014) assuming infinite sample population. All reflections included in the Monte Carlo modeling are shown.

https://doi.org/10.1017/S0885715624000484 Published online by Cambridge University Press

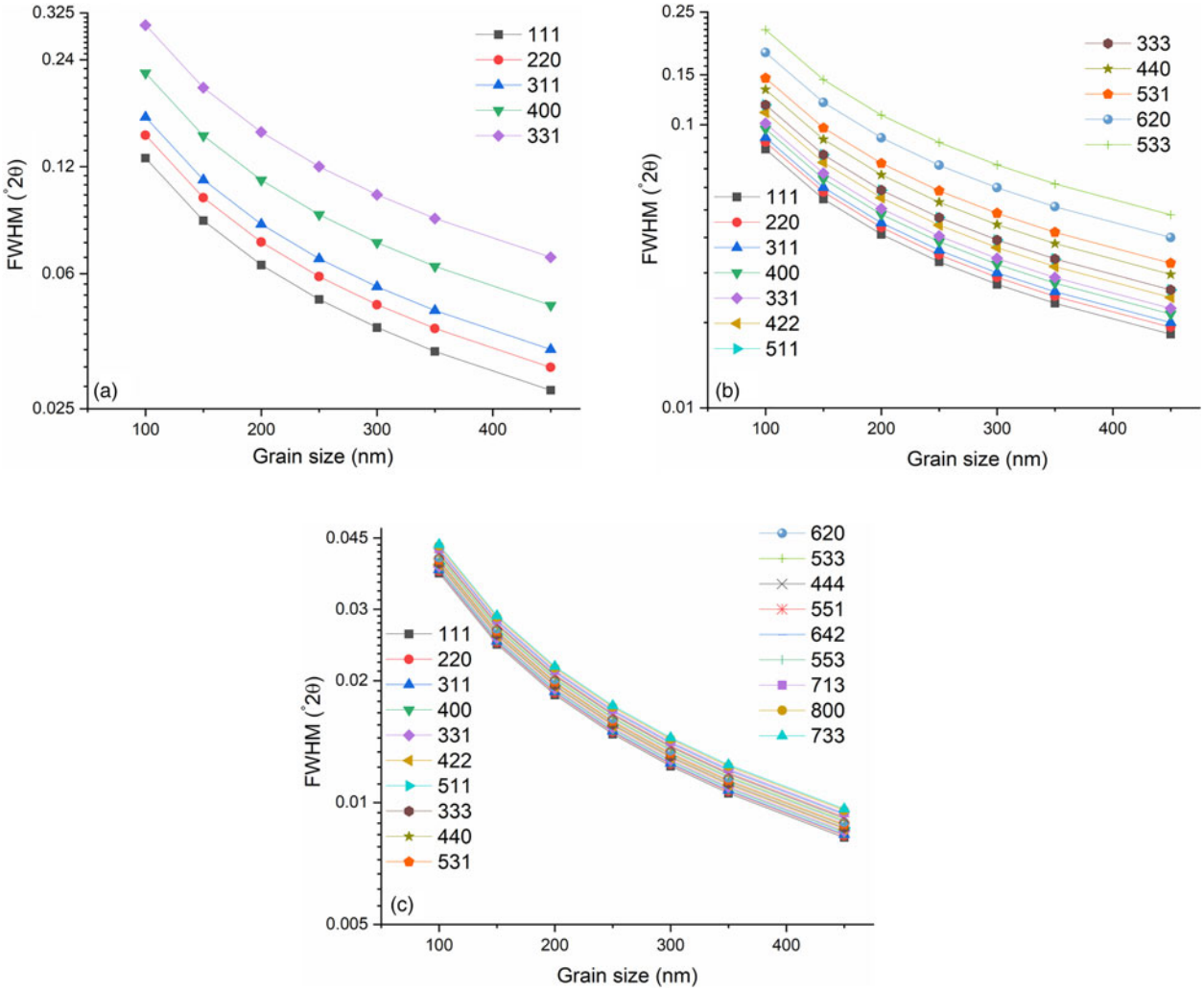

Figure 8. FWHM values of the reflections utilized in sampling simulations with Cr (a), Cu (b), and Mo (c) $K\alpha$ wavelengths, respectively.

radiation, respectively, along with the expected values computed using Eq. (17). The following points can be observed:

1. For a given experiment (fixed Scherrer crystallite size, D, and wavelength, λ) reflection multiplicity, m_{hkl}, determines diffracting crystallite fractions for individual reflections; $(N_G^*/N_G)_{hkl}$ are identical for reflections with identical multiplicities independent of the reflection angle.
2. For powders with crystallites larger than 300 nm, reflections with low multiplicities, such as $h00$, hhh, and $hk0$, have very small sampling fractions ($0.01\ll$) when the higher energy (small λ) monochromatic X-rays were used.

In Figure 9(d), the total diffracting crystallite fractions for the powder patterns, $(N_G^*/N_G)_{ptn}$, and the corresponding expected values [Eq. (17), dashed lines] are plotted. For the three cases simulated, $(N_G^*/N_G)_{ptn}$ values are in the range of 33% for 100 nm crystallites illuminated with Cu$K\alpha$ radiation, to 3.4% for 450 nm crystallites illuminated with Cr$K\alpha$ radiation. We note that these values correspond to complete Debye rings azimuthally integrated to obtain one-dimensional diffraction patterns. For systems utilizing, for example, Bragg-Brentano geometry with parallel-beam slit optics, the corresponding fractions can be two orders of magnitude smaller (Appendix A).

Figure 9(d) also shows that the number of reflections in a powder pattern is an insufficient metric for comparing diffracting crystallite fractions for the whole pattern, $(N_G^*/N_G)_{ptn}$; powder patterns modeled with Cu radiation (12 reflections) had larger $(N_G^*/N_G)_{ptn}$ values than those with Mo radiation (19 reflections) for all Scherrer crystallite sizes.

To compare the sampling efficiency in the simulated powder patterns, we computed the sampling quotient $Q^S_{\lambda_2-\lambda_1}$ [Eq. (21)] for each wavelength pair from the numerical models and compared them to the values predicted by this equation. The results are summarized in Figure 10. As expected, $Q^S_{\lambda_2-\lambda_1}$ is independent of particle size. We observe that, while switching from Cr to Cu or Mo radiation improves sampling efficiency significantly, switching from Cu to Mo radiation decreases the sampling efficiency by ~20% even though the powder pattern utilizing Mo radiation included seven more reflections.

2. Multi-wavelength analysis

Our formalism can be extended to experiments that have access to pink incident beams where one can use an energy-dispersive detector, or an appropriate set of adjustable monochromators, to easily obtain diffraction patterns for a set of selected wavelengths. In this case, Eq. (17) is modified with

https://doi.org/10.1017/S0885715624000484 Published online by Cambridge University Press

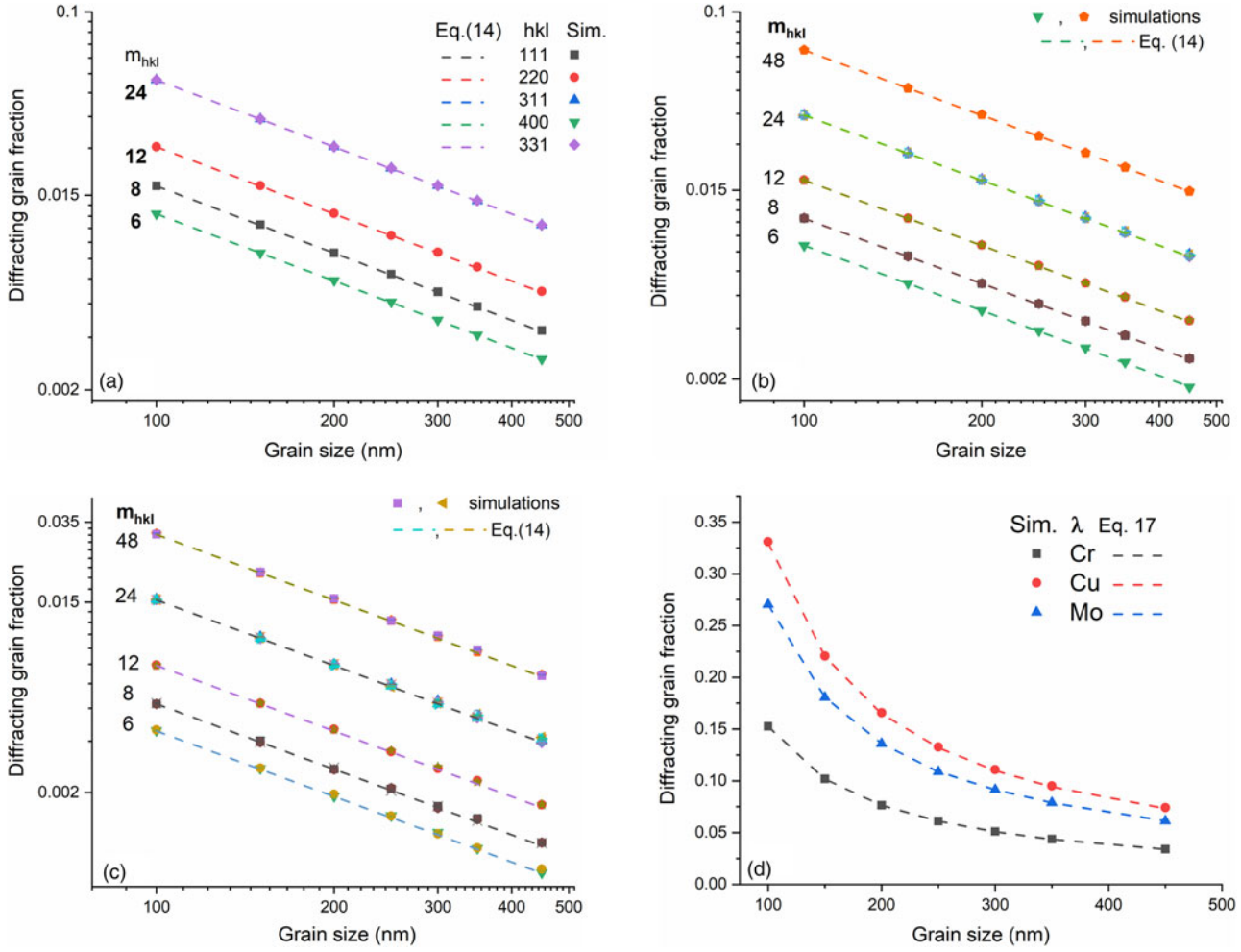

Figure 9. Variation of modeled diffracting crystallite fractions for individual reflections, $(N_G^*/N_G)_{hkl}$ with Cr (a), Cu (b), and Mo (c) radiation. The total crystallite fractions, $(N_G^*/N_G)_{ptn}$, diffracting into the respective powder patterns are plotted in (d). The dashed lines in (d) were computed using Eq. (17).

an additional sum over all wavelengths:

$$E[N^{ptn}_{tot,PB,\lambda_{pn}}] = \left(\frac{K'N_G}{D}\right)\sum_j\sum_i m_{(hkl)_i}\lambda_j \qquad (23)$$

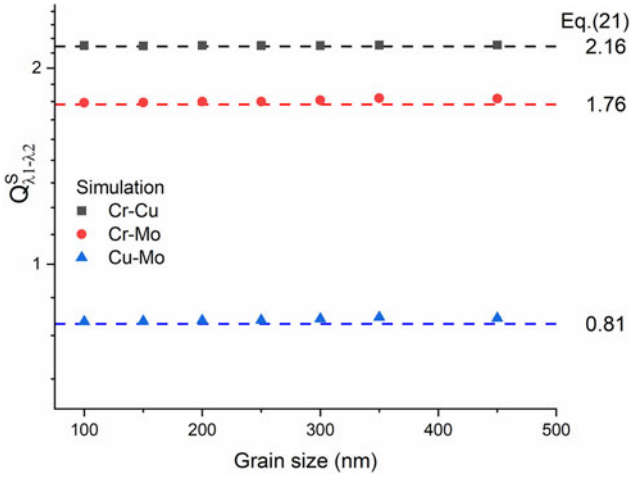

Figure 10. The sampling quotient $Q^S_{\lambda_2-\lambda_1}$ [Eq. (21)] plotted as a function of crystallite size for each wavelength pair from the numerical models. Analytical predictions are shown by dashed lines.

The fraction of diffracting crystallites is given by:

$$\frac{E[N^{ptn}_{tot,PB,\lambda_{pn}}]}{N_G} = \left(\frac{K'}{D}\right)\sum_j\sum_i m_{(hkl)_i}\lambda_j \qquad (24)$$

For our simulations with three wavelengths, the sum in Eq. (23) becomes:

$$\frac{E[N^{ptn}_{tot,PB,\lambda_{pn}}]}{N_G} = \left(\frac{K'}{D}\right)\left[\left(\sum_1^5 m_{(hkl)_i}\sum_1^3\lambda_j\right) + \left(\sum_6^{12} m_{(hkl)_i}\sum_2^3\lambda_j\right) + \left(\lambda_3\sum_{13}^{19} m_{(hkl)_i}\right)\right] \qquad (25)$$

The first five reflections are accessible in the powder patterns simulated with all three wavelengths, λ_1, λ_2, and λ_3 (Table I), reflections 6–12 are accessible for λ_2 and λ_3, while reflections 13–19 are accessible only with λ_3. We note that, in the geometry shown in Figure 1, different crystallites contribute to Debye-Scherrer halos of the higher orders of a given reflection. This is not the case for all diffraction geometries: for radial scans with the Bragg-Brentano geometry, Eqs. (23) and (24) cannot be used without modification

https://doi.org/10.1017/S0885715624000484 Published online by Cambridge University Press

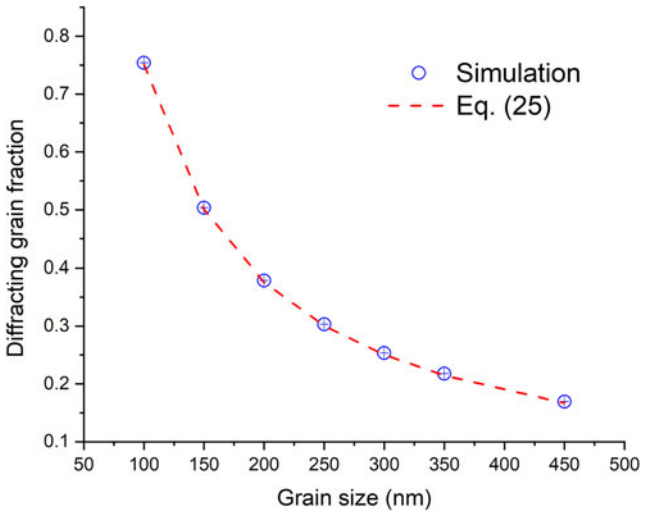

Figure 11. Fraction of diffracting crystallites for a hypothetical multi-wavelength experiment utilizing three wavelengths in the incident beam. The symbols are simulation results, where the error bars are comparable in size to the symbols. The dashed line is computed using Eq. (25).

since this scan type limits the orientation of the diffracting plane vectors to those parallel with the sample surface normal (Appendix A).

Figure 11 shows the fraction of crystallites contributing to the information volume of a powder diffraction experiment when our hypothetical sample is illuminated with a pink X-ray beam and the three wavelengths shown in Table I are selected, sequentially, with appropriate monochromators. Here the symbols are results obtained from the simulation, and the dashed line is calculated from Eq. (24). When full Debye rings are recorded, the fraction of crystallites contributing to the diffraction pattern is in the range of 0.75 and 0.16, for powders consisting of 100 and 450 nm diameter crystallites, respectively. The corresponding sampling fractions achieved when Cu$K\alpha$ radiation was used by itself were ~0.34 and 0.08, respectively. We observe that pooling the information volumes from all three wavelengths improves sampling by almost a factor of two for all (Scherrer) crystallite sizes.

IV. DISCUSSION

The formalism described above is only applicable to an ideal diffraction experiment utilizing the transmission geometry shown in Figure 1, where a monochromatic, plane-wave incident beam illuminates all crystallites in the beam path, and the (kinematic) diffracted signal is recorded on an area detector which captures complete Debye rings for all (basis-permitted) reflections. Under these conditions, in a given experiment with fixed Scherrer size, the sampling parameter, $C_\lambda = \lambda \sum_i m_{(hkl)_i}$ [Eq. (18)] is the primary variable governing diffraction sampling. This parameter shows, trivially, that for fixed λ, sampling statistics are improved if one includes more reflections, especially those with higher m_{hkl}. If the angular range of the experiment does not permit accessing such reflections, one can use higher energy (smaller λ) to access more of the reciprocal space. In such cases, maximizing C_λ becomes an optimization problem; the presence of more reflections at a smaller λ does not necessarily improve particle sampling (Figure 9(d)). If one records patterns for several (monochromatic) wavelengths, the (multi-pattern) sampling parameter is significantly improved and includes a sum over these λ:

$$C_\lambda^{mp} = \sum_j \sum_i m_{(hkl)_i} \lambda_j \tag{26}$$

Here, the inner sum is over those reflections that are accessed for each wavelength λ_j. In the case of an incident beam where the wavelength distribution is continuous over some range (such as time-of-flight (TOF) thermal-neutron diffraction experiments), it might be possible to replace the outer sum with suitable integrals. This point is under investigation (As the number of wavelengths increases, some grains will contribute to more than one Debye-Scherrer cone (Stoica et al., 2019). To obtain the proper average values of direction-dependent parameters from diffraction analysis requires taking such oversampling into account. This is a non-trivial problem and will be reported later.).

In our ideal treatment, the effects of incident beam divergence, photo-electric absorption, instrumental broadening, fractional capture of Debye rings and other, similar, geometric effects are neglected. If the (monochromatic) incident beam has finite divergence, more grains will satisfy the diffraction condition, but the number of grains around the exact Bragg angle will have minimal changes (Appendix A). These effects can be taken into account by changing the range factor, s [Eq. (12)], which is a multiplier in all subsequent equations. Consequently, the trends predicted by Eqs. (12)–(24) would not change, while absolute magnitudes of diffracting grain fractions might. Similar considerations apply to the fractional capture of Debye rings: provided that identical fractions of multiple rings are recorded, and azimuthally integrated into a one-dimensional powder pattern, the predicted trends should be valid. We note that, in real experiments, the effects of instrumental peak broadening, peak asymmetry, along with any strain-broadening should be removed from the (measured) peak profile(s) using standard deconvolution methods (Azâroff, 1974; Jenkins and Snyder, 1996) if experimental FWHM values are to be used for computing the acceptance angles of the crystallites.

The effect of photo-electric absorption will be more significant in the formalism described here, especially in those cases where the incident beam cannot penetrate the entire sample thickness, and different volumes within the sample contribute to particular reflections. In such cases, the number of illuminated grains for each reflection might be different, and Eqs. (14)–(16) should be modified using the approaches given in past literature (De Wolff, 1959; De Wolff et al., 1959; Noyan and Kaldor, 2004; Ida et al., 2009). We note that these modifications only involve the specification of the number of illuminated crystallites, N_G; all other considerations are unchanged. Similar modifications would be needed in specifying N_G if some of the selected wavelengths in a polychromatic beam could not penetrate the entire sample, or in experiments where beam-hardening effects are significant. However, if all λ are energetic enough to penetrate the entire sample thickness, the trends predicted by Eqs. (14)–(23) would be unchanged.

Finally, particle sizes, D, appearing in Eqs. (12)–(20) are only valid in the kinematic diffraction range. This has a lower limit at approximately 100 nm where particle size broadening permits a single grain to contribute multiple active poles to the reflection band (Öztürk et al., 2014, 2015; Öztürk and Noyan, 2017). Dynamic diffraction effects impose an upper limit at

https://doi.org/10.1017/S0885715624000484 Published online by Cambridge University Press

the dynamical extinction depth of (perfect) crystals, ξ_D, beyond which the shape of the diffraction peak tends to the Darwin-Prins profile; the breadth of this peak profile, and the corresponding band-pass of the (perfect) crystallite, can no longer be described by the Scherrer equation (Authier, 2003). We note that ξ_D for a given reflection is weakly dependent on the incident wavelength and is less than $\sim$5 μm for most reflections from perfect crystals. Thus, experimental results of articles which use larger (perfect) crystallites in evaluating intensities and particle statistics might require some care in interpretation.

V. CONCLUSION

We have derived and validated a set of simple equations, based on the Lorentz-Scherrer equation and Bernoulli statistics, for estimating the fraction of crystallites (and the associated uncertainty parameters) contributing to all finite Bragg peaks of a powder pattern obtained in the transmission geometry with an area detector. These equations are applicable only for kinematically scattering crystallites, with coherently scattering domain sizes along the scattering vector between 100 nm and 5 μm. This formalism can be extended to other types of detectors in this geometry, or for other diffraction geometries (Appendix A), and used in optimizing powder diffraction experiments using X-rays or constant wavelenght (CW) neutrons, from stationary, solid polycrystalline specimens for sampling efficiency. Our results show that comparing sampling efficiencies of different wavelengths in acquiring powder diffraction patterns from a given sample cannot be based solely on comparing the number of reflections included in each pattern. For such comparisons, the sampling quotient $Q^S_{\lambda_1\rightarrow\lambda_2}$ [Eq. (21)] might provide a first-order estimate. Finally, it might be useful if studies utilizing powder diffraction data for information-volume sensitive parameters, such as lattice strain/residual stress analysis and texture measurements, reported the fraction of grains sampled in their experiments, and discussed why this fraction was deemed satisfactory, from a sampling perspective, for any continuum-mechanics based analysis. Such reporting would be facilitated if our formalism and/or its extensions for specific measurement geometries were included in standard Rietveld codes, where most parameters required for such computations are readily available.

ACKNOWLEDGEMENTS

The authors state that there are no conflicts of interest associated with this work. All reported simulations were coded and generated by M.A.N. I.C.N. derived the analytical formalism equations, computed relevant parameters without being informed of the simulation results, and performed the final comparisons. I.C.N. acknowledges the support of Columbia University for supporting his work in this area.

REFERENCES

Alexander, L. E., H. P. Klug, and E. Kummer. 1948. "Statistical Factors Affecting the Intensity of X-Rays Diffracted by Crystalline Powders." *Journal of Applied Physics* 19 (8): 742–53.

Authier, A. 2003. *Dynamical Theory of X-Ray Diffraction*. Oxford University Press.

Azâroff, L. V. 1974. *X-ray Diffraction*. McGraw-Hill.

Bijvoet, J. M., W. G. Burgers, G. Hèagg, and International Union of Crystallography. 1969. *Early Papers on Diffraction of X-Rays by Crystals*. Published for the International Union of Crystallography by A. Oosthoek.

Buerger, M. J. 1940. "The Correction of X-Ray Diffraction Intensities for Lorentz and Polarization Factors." *Proceedings of the National Academy of Sciences of the United States of America* 26 (11): 637–42.

Buerger, M. J., and G. E. Klein. 1945. "Correction of X-Ray Diffraction Intensities for Lorentz and Polarization Factors." *Journal of Applied Physics* 16 (7): 408–18.

Cheary, R. W., A. A. Coelho, and J. P. Cline. 2004. "Fundamental Parameters Line Profile Fitting in Laboratory Diffractometers." *Journal of Research of the National Institute of Standards and Technology* 109: 1–25.

Cullity, B. D. (1978) *Elements of X-Ray Diffraction*. Addison-Wesley Series in Metallurgy and Materials, 2nd ed. Addison-Wesley.

Degen, T., M. Sadki, E. Bron, U. König, and G. Nénert. 2014. "The HighScore Suite." *Powder Diffraction* 29 (S2): S13–18.

De Wolff, P. M. 1959. "Particle Statistics in X-Ray Diffractometry: I. General Theory." *Applied Scientific Research, Section B* 7 (1): 102–12.

De Wolff, P. M., J. M. Taylor, and W. Parrish. 1959. "Experimental Study of Effect of Crystallite Size Statistics on X-Ray Diffractometer Intensities." *Journal of Applied Physics* 30 (1): 63–69.

Elton, N. J., and P. D. Salt. 1996. "Particle Statistics in Quantitative X-Ray Diffractometry." *Powder Diffraction* 11 (3): 218–29. doi:10.1017/S0885715600009155.

Ida, T., T. Goto, and H. Hibino. 2009. "Evaluation of Particle Statistics in Powder Diffractometry by a Spinner-Scan Method." *Journal of Applied Crystallography* 42 (4): 597–606.

Ida, T., T. Goto, and H. Hibino. 2011. "Particle Statistics in Synchrotron Powder Diffractometry." *Zeitschrift für Kristallographie Proceedings* 1: 69–74.

Jenkins, R., and J. L. de Vries. 1978. Particle statistics in X-ray diffractometry. In: *Worked Examples in X-Ray Analysis*. Philips Technical Library. Palgrave, pp. 61–63. https://link.springer.com/chapter/10.1007/978-1-349-03534-2_24#citeas

Jenkins, R., and R. L. Snyder. 1996. *Introduction to X-ray Powder Diffractometry*. John Wiley & Sons.

Johnson, N. L., A. W. Kemp, and S. Kotz. 2005. *Univariate Discrete Distributions*. John Wiley & Sons.

Klug, H. P., and L. E. Alexander. 1974. *X-ray Diffraction Procedures: For Polycrystalline and Amorphous Materials*. Wiley-Interscience.

Noyan, I. C., and S. K. Kaldor. 2004. "Measurement Volume Considerations in X-Ray Microdiffraction Stress Analysis." *Powder Diffraction* 19 (2): 104–9.

Noyan, İ. C., and H. Öztürk. 2022. "Lower Uncertainty Bounds of Diffraction-Based Nanoparticle Sizes." *Journal of Applied Crystallography* 55 (3): 455–70.

Noyan, I. C., P. C. Wang, S. K. Kaldor, J. L. Jordan-Sweet, and E. G. Liniger. 2000. "Divergence Effects in Monochromatic X-Ray Microdiffraction Using Tapered Capillary Optics." *Review of Scientific Instruments* 71 (5): 1991–2000.

Öztürk, H., and I. C. Noyan. 2017. "Expected Values and Variances of Bragg Peak Intensities Measured in a Nanocrystalline Powder Diffraction Experiment." *Journal of Applied Crystallography* 50 (5): 1307–22.

Öztürk, H., H. Yan, J. P. Hill, and I. C. Noyan. 2014. "Sampling Statistics of Diffraction from Nanoparticle Powder Aggregates." *Journal of Applied Crystallography* 47 (3): 1016–25.

Öztürk, H., H. Yan, J. P. Hill, and I. C. Noyan. 2015. "Correlating Sampling and Intensity Statistics in Nanoparticle Diffraction Experiments." *Journal of Applied Crystallography* 48 (4): 1212–27.

Schdanow, H. S. 1935. "Bestimmung der Kornzahl im Bereiche von 1 bis 100 μ auf Grund der Debye-Scherrer-Aufnahmen." *Zeitschrift für Kristallographie - Crystalline Materials* 90 (1–6): 82–92.

Şeren, M. H., D. C. Pagan, and I. C. Noyan. 2023. "Representative Volume Elements of Strain/Stress Fields Measured by Diffraction Techniques." *Journal of Applied Crystallography* 56 (4): 1144–67.

Smith, D. K. 1991. "Particle Statistics and Whole-Pattern Methods in Quantitative X-Ray Powder Diffraction Analysis." *Advances in X-ray Analysis* 35A: 1–15.

Smith, D. K. 2001. "Particle Statistics and Whole-Pattern Methods in Quantitative X-Ray Powder Diffraction Analysis." *Powder Diffraction* 16 (4): 186–91.

Stoica, G. M., A. D. Stoica, K. An, D. Ma, S. C. Vogel, J. S. Carpenter, and X. L. Wang. 2014. "Extracting Grain-Orientation-Dependent Data from In Situ Time-of-Flight Neutron Diffraction. I. Inverse Pole Figures." *Journal of Applied Crystallography* 47 (6): 2019–29.
Taylor, A. J. P. 1961. *X-Ray Metallography*. John Wiley & Sons.
Uspensky, J. V. 1937. *Introduction to Mathematical Probability*. McGraw-Hill.

APPENDIX A

The formalism described by Eqs. (12)–(24) is strictly applicable only when a parallel incident beam is used and entire Debye rings are captured using area detectors. These conditions are best approximated in experiments utilizing high-energy beamlines in synchrotron sources. Most conventional powder diffraction measurements utilizing laboratory sources, such as the ubiquitous Bragg-Brentano (B–B) geometry, take pseudo-one-dimensional cuts through the rings, either horizontally or vertically, depending on the diffractometer geometry (Figure 12). In such cases, crystallite fraction contributing intensity to a given Bragg peak is proportional to the fraction of the corresponding Debye ring circumference captured by the receiving slit of the diffracted beam optics (Noyan and Kaldor, 2004):

$$f_S = \frac{L_S}{2\pi R \sin 2\theta_B} \tag{A1}$$

Since the diffractometer radius R is usually much greater than the slit height, L_S, the fraction of diffracting grains for B–B scans employing a parallel incident beam can be much smaller than the fractions shown in Figure 9. In addition, for symmetric (radial) scans, the grains contributing to any reflection, hkl, must have their $\{hkl\}$ planes parallel to the sample surface. This will further decrease the fraction of crystallites contributing to the powder pattern since some subsets of crystallite groups contributing to the higher orders of a given reflection are identical. (The illuminated volume, the product of the spot area on the specimen and the penetration depth, is constant for a symmetric B–B scan: as θ increases, the decrease in the area of the incident beam spot on the sample surface is balanced by an increase in the penetration depth. If the Scherrer size is larger than the X-ray penetration depth, the decrease in spot size might decrease the number of diffracting grains for the higher-order reflection.) Thus, including higher-order reflections in the powder pattern might not provide additional crystallite volumes to the measurement.

On the other hand, if parafocussing Bragg-Brentano geometry with a curved specimen is utilized, more crystallites illuminated by the divergent incident beam will satisfy the Bragg condition (Figure 13). In this case, the angular breadth of the "reflection band" will be much wider than the band-pass of the individual crystallites, and $\Delta\theta$ in Eq. (9) can be replaced by the beam divergence angle, α:

$$p^*_{hkl} \cong \frac{1}{2}\alpha\, m_{hkl}\cos\theta_{B,hkl} \tag{A2}$$

This will significantly increase the fraction of grains contributing (focused) diffracted beams into the detector. However, since the distribution of incident intensity within the divergent beam fan decreases monotonically as one moves away from the central ray (Noyan et al., 2000), the number of grains contributing maximum intensity to the Bragg peak can be quite small. In an actual scanning microbeam experiment with a divergent beam ($\alpha = 0.36°$) illuminating a large-grained Cu sample (optical grain size 29 ± 8 mm), approximately 120 grains, out of ~4000 illuminated grains, contributed finite intensity to the 222 reflection. Of these 120, only five contributed intensities exceeding half of the maximum intensity (Noyan and Kaldor, 2004). We conclude that the fraction of diffracting grains obtained from Eq. (A2) is an upper limit.

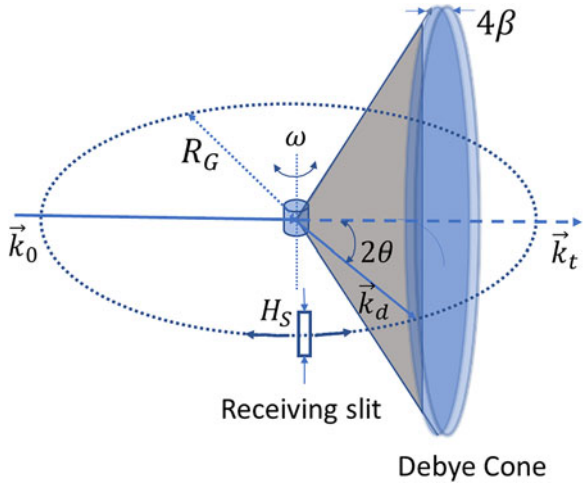

Figure 12. Pseudo-one-dimensional strip of a Debye cone sampled by a receiving slit in the Bragg-Brentano geometry. The incident and diffracted beam vectors define the diffractometer plane, which also contains the diffracting plane normal. For the best angular resolution, the width of the receiving slit in the diffractometer plane should be much smaller than the FWHM of the Bragg peak, β. For symmetric scans, the sample rotation angle, ω, is exactly half of the detector angle, 2θ, for $0° \le 2\theta \le 180°$.

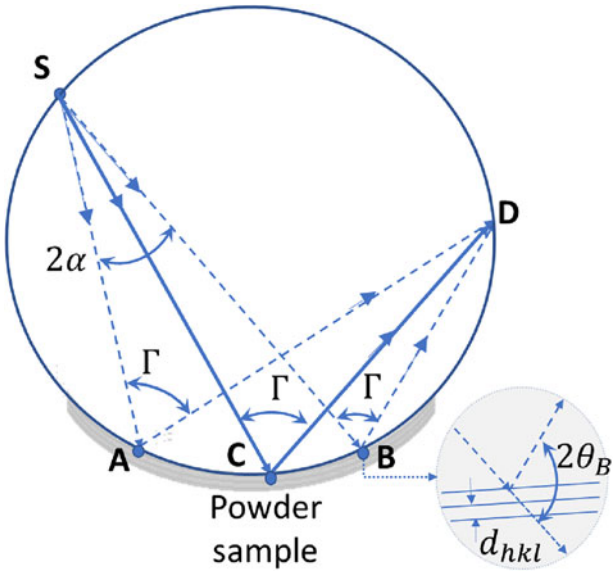

Figure 13. Parafocussing geometry for a Bragg-Brentano diffractometer. Only the focusing circle is shown. All diffracted rays from grains within the arc-segment **AB** of the (curved) polycrystalline specimen will be focused at the detector **D**. The inset shows the diffraction geometry at point **B**. The central ray **SC** will be the most intense ray of the divergent incident beam fan. The angular variable, $\Gamma_B = (\pi/2) - \theta_B$, is identical to Γ_B defined in Figure 1. For illustration purposes, the (arc) length of the (curved) specimen is highly exaggerated.

https://doi.org/10.1017/S0885715624000484 Published online by Cambridge University Press